Balance of Efficiency and Security-influence on Slurry Transport from the Diffusion of Flow Passages of a Deep-sea Mining Pump

Z. Zhu[1], Y. Lv[1], X. Su[1,2†], J. Zhang[1], R. Wang[1], W. Lu[1] and J. Sun[3]

[1] Zhejiang Sci-Tech University, Hangzhou 310000, China
[2] Changsha Research Institute of Mining and Metallurgy, Co. Ltd., Changsha 410000, China
[3] Tengda Construction Group LTD, Taizhou 318000, China

†*Corresponding Author Email: suxianghui@sina.com*

ABSTRACT

Slurry transport pumps, the central equipment of deep-sea mining (DSM) systems, provide the lifting power required for lifting mineral ores from the seafloor to the surface. The current technical challenges are associated with transport security and the economic aspects of coarse ore particles in pumps and pipelines. This paper focuses on the transportation characteristics of slurry pumps and uses theoretical methods, numerical calculations, and experimental methods to identify a feasible working mode. The geometric parameters of impeller channels in pump hydraulics significantly influence the migration properties of particles which in turn affects the overall security and economy of the system. The ratio of the impeller cross-sectional area F_2/F_1 (F_1: cross-sectional area of the impeller outlet; F_2: cross-sectional area of the impeller inlet) affects the particle passing capacity but negatively impacts pump efficiency. The percent of particles in the excellent passage interval of 0.2 s to 0.25 s increases from 25 to 43% when the number increases from 1.57 to 2.51. The pump behavior increases of the head by 5–10 m, and the efficiency decreases by 5–10%. So, the recommended span of F_2/F_1 is 1.57–2.00, and satisfying particle passing ability and efficiency can be achieved in this range. This study can provide a reference for the commercial transportation of slurry ores for deep-sea mining systems.

1. INTRODUCTION

Deep-sea minerals (such as polymetallic nodules and sulfides) deposited on the seabed have stimulated great interest in scientific fields since the 1960s. Particularly, land-based rare elements such as nickel, cobalt, and samarium have attracted immense attention, and these are essential for the sustainable development of clean energy (Glasby et al., 2015). These are considered valuable resources for advancing technologies and have limited reserves on land. A large amount of these minerals are found in the seabed of the Pacific and Indian Oceans. For example, submarine reserves of nickel account for 99.9% of total nickel reserves, while land reserves of cobalt account for less than 0.02% of the total reserves (Sharma 2011). With the development of the new energy industry and the depletion of land resources, interest in deep-sea mineral resources is increasing worldwide. Research in the field has resulted in the development of deep-sea mining (DSM) technology and equipment.

This equipment system collects and transports mineral resources from the seabed to the surface. Ensuring the reliability and efficiency of underwater work is critical as the deep-sea environment is extremely hostile.

Mining–lifting system consists of four parts, as shown in Fig. 1. The flexible hose at the bottom connects the collector and buffer, which is used for quantitative feeding and concentrating slurry. Thousands of meters of risers are responsible for lifting, and a slurry pump is installed in the middle of the risers to provide power for the lifting system. The slurry-delivering characteristics of the system are influenced by the operating flow rate, water depth, mineral concentration, nodule lift property, and the performance of the slurry transport pumps (Fig. 2) (Wang 2015), which often operate at a variable frequency to suit the diverse operating conditions. Despite this, pump clogging events frequently occur, as shown in Fig. 3 (Li et al., 2020). Thus, it is important to develop pumps that ensure safety. The efficiency of the existing slurry pumps is lower than that of the pumps operated under common situations.

Nomenclature

C_v	volume concentration of the slurry	P_{eff}	useful work of the pump
F_1	cross-sectional area of the impeller outlet	Q	flow rate of the pump
F_2	cross-sectional area of the impeller inlet	S_f	nodule particle shape factor
F_i	gravitational volume force	v_i	component of the velocity vector
$F_{n,ij}$	normal force between particle i and particle j	W_{gt}	critical settling velocity of the nodule population
$F_{\tau,ij}$	tangential force between particle i and particle j	W_t	critical settling velocity of single particles of nodules
g	acceleration of gravity	ρ_0	clear water density
J_m	slurry hydraulic slope	ρ_s	nodule density
H	head of the pump	ρ_{sw}	seawater density
h_f	frictional head loss	Δ	pipe roughness
h_w	local head loss	ρg_i	gravitational volume force
I_i	moment of inertia	τ_{ij}	viscous stress tensor caused by fluid motion.
i	i direction of the coordinate system	CFD	Computational Fluid Dynamics
M_i	the rolling friction torque.	DEM	Discrete Element Method
P	the static pressure	DSM	Deep-Sea Mining
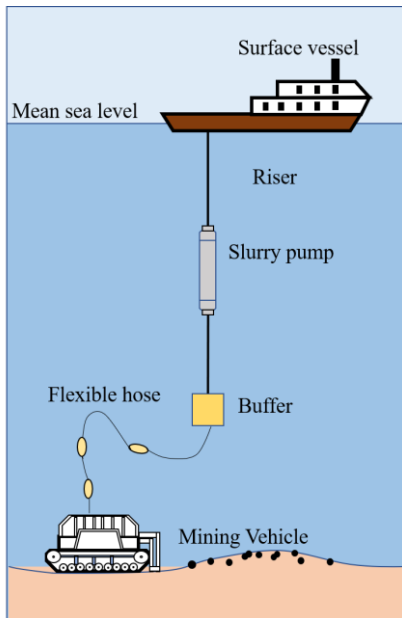
Fig. 1. Schematic diagram of the DSM system.

Fig. 2. Lifting system characteristics (Wang, 2015)

Fig. 3. Pipe blockage in pumps (Li et al., 2019).

A typical slurry pump (420 m3/h; 270 m; particle concentration: 5–10%) has an efficiency of 50% at rated points, which results in huge energy consumption in large-scale commercial mining conditions (Wang et al., 2022). Therefore, this paper focuses on the design of slurry transport pumps, particle movement, and fluid profiles to address the safety and economic parameters of the transfer system.

This paper presents a current state description from three aspects: the design of the pump, two-phase flow within a pump, and particle motion characteristics.

Several attempts have been made to modify the impeller structure of multi-phase hydraulic systems. Tao et al. (2017) changed the thickness of impeller vanes so that the extent of changes in the pressure at the vane's
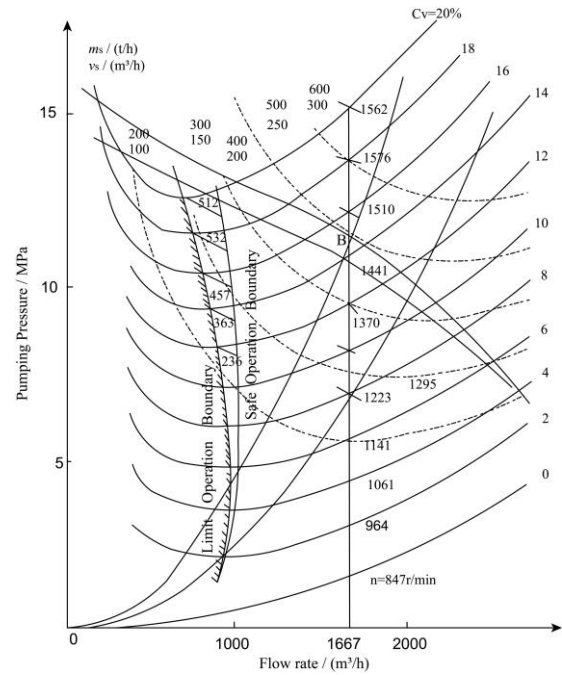
leading-edge increases and that at the trailing edge decreases. The particles at the rear impeller were dispersed under these conditions. Abdolahnejad et al. (2021) investigated the best number and length of the splitter vanes and found that 6% and 62.8% of the main vane, respectively. Matlakala et al. (2019) calculated and compared the impact of different impeller diameters on

pump performance and revealed that the reduction of the impeller resulted in a reduction in the extent of power consumption realized. Liu et al. (2019a) designed different guide vanes with various blade angles to change the magnitude of particle fluctuations, thereby reducing the extent of wear of guide vanes. Kim et al. (2019) studied the coefficient of the volume proportion of a blade in the flow channel, found the best proportion coefficient of the blade, and obtained the positive proportion relationship between the pressurization capacity and the proportion coefficient. Sha and Hou (2012) found the relationship between the blade thickness and the change rule of the hydraulic characteristic curve of the pump by changing the structural parameters, and concluded that the thin blade has excellent performance but poor corrosion resistance, and explained the reason why the blade thickness increases and the pump performance decreases.

Solid–liquid two-phase flow systems were extensively analyzed by numerous researchers. Tang and Kim (2020) reported that the smaller particles in the single-channel pump have a broader speed range and limiting velocity, unlike larger particles that were characterized by greater contact force. Dong et al. (2017) argued that the crystal particles in the pump were evenly distributed at the inlet. The particles entered the impeller, and it was observed that the density was low on the suction side of the blade and high on the pressure side. The CFD–DEM method was used for analysis. Liu et al. (2019b) reported that an increase in the pump's flow rate could improve the particles' fluidity and reduce the pump's wear. Li et al. (2018) argued that increasing the impeller speed can improve the passing rate of the particles and reduce the extension of collision between particles.

Many researchers have conducted in-depth studies on particle movement. The relationship between particle concentration and particle size, and wear in the pump was investigated by Yang et al. (2013). Liu et al. (2019c) found that when the particle concentration was 10%, the pump ran stably, and good efficiency and head space were achieved. They used the CFX numerical simulation method to arrive at the results. Hong et al. (2016) concluded that if the profile of the blades resembled the traces of the movement of the particles, the particles would minimize the wear of the blades. Tarodiya and Gandhi (2019) suggested that the pump head space and efficiency decreased with an increase in particle size and concentration. Wen et al. (2019) considered the impact of particle sizes on the two-phase flow property, and their analysis revealed that particles of size 10 mm adapted well to particle motion.

Previously reported results on the design of pumps, the solid–liquid two-phase flow, and solid-phase properties served as good reference points for this research. However, studies on the impact of the impeller inlet and outlet area ratio on the particle movement were rarely studied, and this ratio had a prominent impact on the particle migration properties in the slurry pump. This, in turn, affected the safety and efficiency of slurry transport pumps. Therefore, this paper uses a typical slurry pump to explore the correlations between internal solid–liquid two-

phase flow and external behaviors and study the influence of geometric parameters.

2. MATHEMATICAL AND PHYSICAL MODEL OF SLURRY PUMP

2.1 Parameters of Slurry Transport Pumps

The properties of a slurry transport pump have been presented. The flow rate was 420 m3/h, the headspace was 270 m, the rotating speed was 1450 rpm, and the specific speed was 104. The water flow rate of the designed model pump (Fig. 4) was 120 m3/h, the headspace was 40 m (2 stages), and the speed was 1475 rpm. The basic geometric parameters are shown in Table. 1.
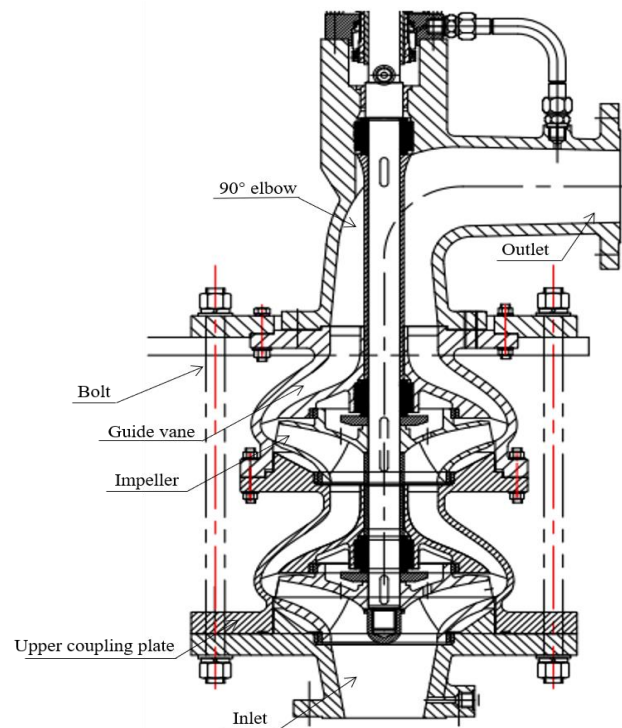
(a) Schematic diagram of the slurry pump
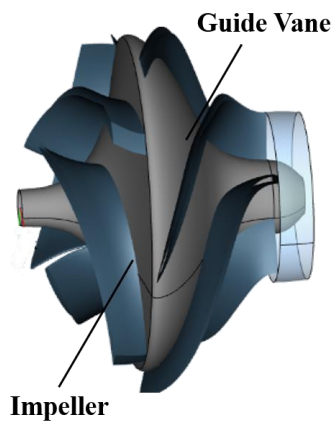
(b) Schematic diagram of a single hydraulic stage of slurry pump

Fig. 4. Model of slurry pump

Table 1 Geometric parameters of a slurry pump.

Geometric parameters	Original pump(model1)		
	Impeller Parameters	Geometric Parameters	Guide vane parameters
Inlet diameter (mm)	135	Inlet diameter (mm)	276
Outer diameter of impeller (mm)	272	Inlet width (mm)	26
Outlet width (mm)	25	Axial length (mm)	127.5
Number of blades	4	Number of blades	5
Wrap angle (°)	111~115	Wrap angle (°)	118
Inlet angle (°)	24	Inlet angle (°)	25
Exit angle (°)	26	Exit angle (°)	90
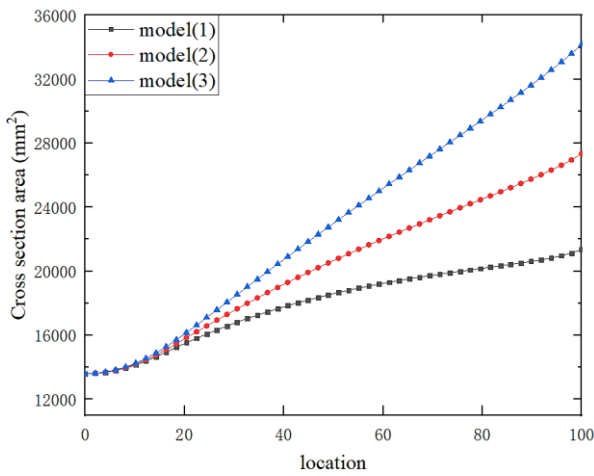
Fig. 5. Changes in the flow area of different models.

The inlet and outlet area ratios of the impeller shaft surface were optimized to clarify the influence of the parameters on particle movement. The cross-sectional area of the impeller inlet and outlet is calculated as follows:
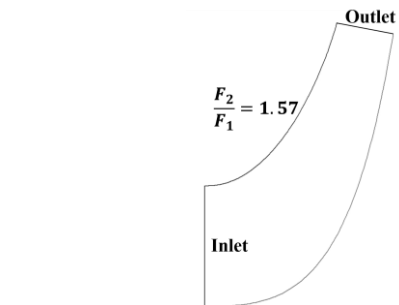
$$F_i = 2\pi D_i b_i \tag{10}$$

Figure 5 shows the variation in flow area for the three comparison models at different F2/F1 ratios (F_1::cross-sectional area of the impeller outlet; F_2::cross-sectional area of the impeller inlet). As shown in Fig. 6, the area ratio of the inlet and outlet of the prototype pump is 1.57, and the ratios corresponding to model 2 and model 3 are 2.00 and 2.51, respectively.
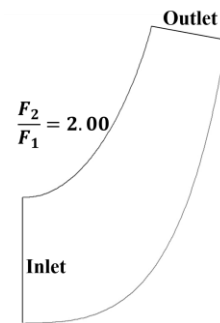
2.2 Particle-Fluid Model

The CFD–DEM method (the computational fluid dynamics–discrete element method), a coupling method, was used to simulate the process. The liquid phase was analyzed using the Navier–Stokes (for momentum) and the continuity equations (for mass conservation). The equations are as follows:

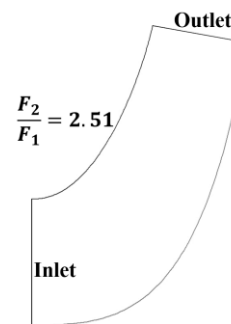$$\frac{\partial \rho}{\partial t} + \frac{\partial}{\partial x_i}(\rho v_i) = 0 \tag{6}$$

$$\frac{\partial}{\partial t}(\rho v_i) + \frac{\partial}{\partial x_j}(\rho v_i v_j) = -\frac{\partial P}{\partial x_i} + \frac{\partial \tau_{ij}}{\partial x_j} + \rho g_i + F_i \tag{7}$$

(a) **model1-original model**

(b) **model2**

(c) **model3**

Fig. 6. Axial view of the impeller of the slurry pump.
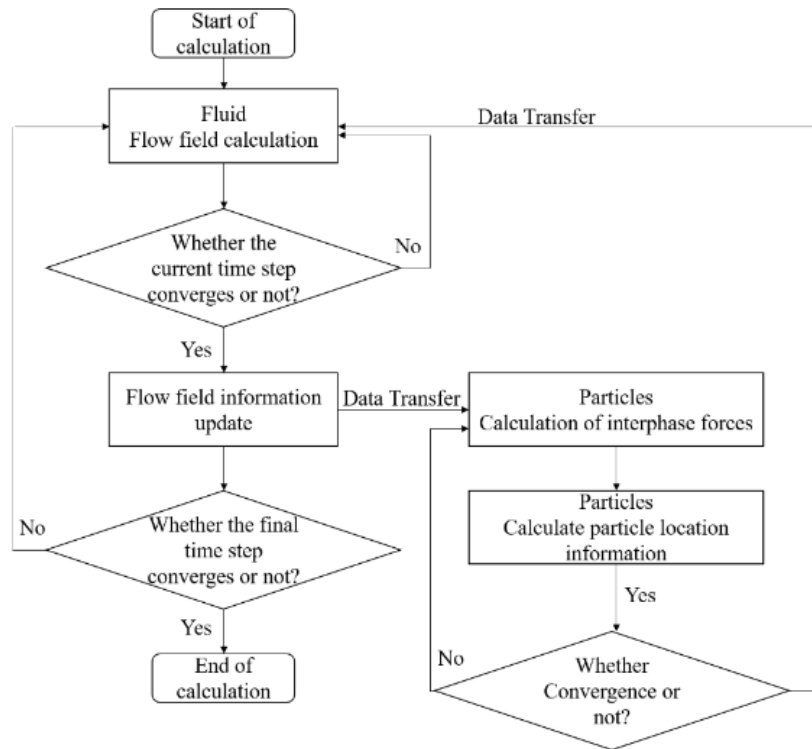
Fig. 7. Flow chart presenting the process associated with CFD–DEM.

Where P is the static pressure, ρg_i and F_i are the gravitational volume force and the external volume force in the *i* direction of the coordinate system, respectively, and τ_{ij} is the viscous stress tensor caused by fluid motion.

The discrete phase can be solved by analyzing the force associated with the particle collision process using the contact model. Newton's second law was used to calculate particle acceleration and update particle velocity and displacement. These are expressed as follows:

$$m_i \frac{dv_i}{dt} = \sum_j \left(F_{n,ij} + F_{\tau,ij} \right) + F_{fp,i} + m_i g \tag{8}$$

$$\frac{d}{dt} I_i \omega_i = \sum_j \left(r_i \times F_{\tau,ij} + M_i \right) \tag{9}$$

Where $F_{n,ij}$ and $F_{\tau,ij}$ are the normal force and tangential force between particle *i* and particle *j*, respectively, $F_{fp,i}$ is the interaction force between the fluid and the particle *i*, I_i is the moment of inertia, and M_i is the rolling friction torque.

In the framework of CFD–DEM (Fig. 7), the equations are solved following the Eulerian–Lagrangian method. The process is to first analyze the fluid at a one-time step and then introduce the local loading force into the particle equation of motion when the calculation converges. The particle information is then returned to the flow field for the next cycle of fluid calculation. The calculation is reiterated until both continuous and discrete phases reach the equilibrium of motion, and finally, the two-way coupling calculation is completed.

According to the working environment and actual working conditions of the slurry pump, the calculation is

reasonably simplified. The basic hypothesis are as follows:

(1) The change of temperature is not considered;

(2) Ignore the compressibility of the fluid;

(3) The solid phase is a rigid spherical particle, and the particle breakage is not considered;

(4) The flow velocity at the inlet of the slurry transport pump is constant;

(5) Particles are randomly distributed at the pump inlet.

2.3 Numerical Procedure

As shown in Fig. 8, the computational domain of the hydraulic model is divided into structured grids using ICEM, and the grid quality is >0.39. The grid independence of eight groups of grids is analyzed based on the prototype model. Grids range from 1.32 million to 6.48 million (Fig. 9). When that number reaches 2.39 million, the total headspace attains stability. A grid size of group 5 can be considered suitable for this paper.
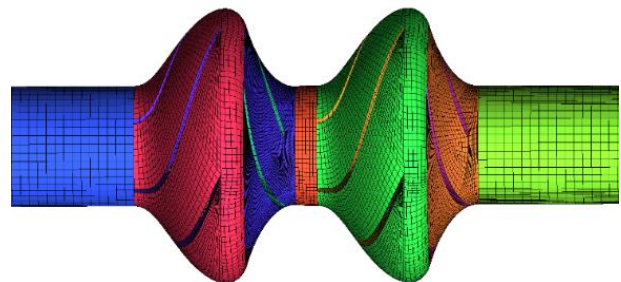

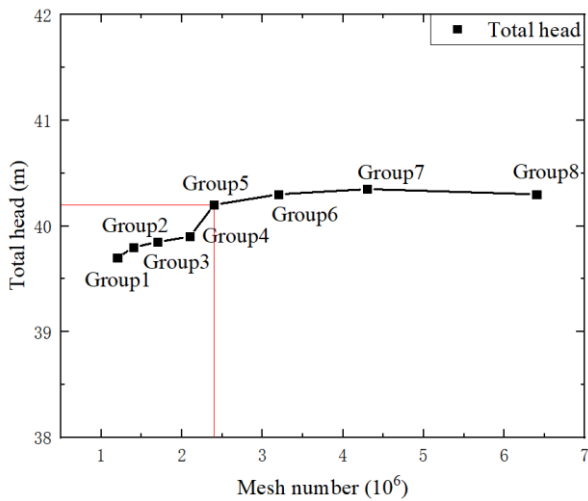**Fig. 8. Grid diagram of the calculation area of the slurry transport pump.**

Fig. 9. Grid independence monitoring.

The fluid simulation process is based on the CFD method. This paper choses a k–ε model with a standard wall function for analysis based on the pressure. Boundary parameters were set to maintain the velocity at the inlet and pressure at the outlet. The pressure was considered as the standard, and the second-order upwind equation and the SIMPLEC format were used for analysis. The time step was set to 3.432e-4s, and the gravitational acceleration was 9.81 m/s^2 (along the negative Z direction).

The particles were simulated based on the DEM method. The particle density and size were 2000 kg/m3 and 10 mm, respectively. Poisson's ratio and shear modulus of particle material are set to 0.4 and 21.3 MPa, respectively. The material density, Poisson's ratio, and shear modulus of the pump material were set to 7800 kg/m3, 0.3, and 70 MPa, respectively. The time step was set to 3.432e-5s, and the gravitational acceleration was still considered as 9.81 m/s2 (along the negative Z direction).

2.4 Experimental Verification

The hydraulic performance of the Model 1 pump (original pump) was experimentally tested. The experimental system is shown in Fig. 10. The system primarily includes motors, mud pumps, valves, solid-liquid separation tanks, filters, etc.

Figure 11 presents a simplified diagram of the operation steps of the experimental system. In a normal circulation system, the solid–liquid two-phase flow property of the particles which first enter the feeding machine is studied. A motor drives the feeding particle machine to send the particles and liquid phase into the pipeline. Finally, a slurry transport pump drives the two-phase flow system to the outlet pipe. The pipeline returns the particles and liquid phases to the particle tank. However, to understand the hydraulic characteristics of the original pump under different working conditions, a three-way valve is added to the circulation system to control the solid-liquid flow of the particles and drive the particles into the solid-liquid separation tank. The process of particle separation is no longer involved in the circulation process. We can understand the characteristics of the pump by adjusting the valve.

(a) Experimental equipment

(b) Experimental slurry transport pump and particles

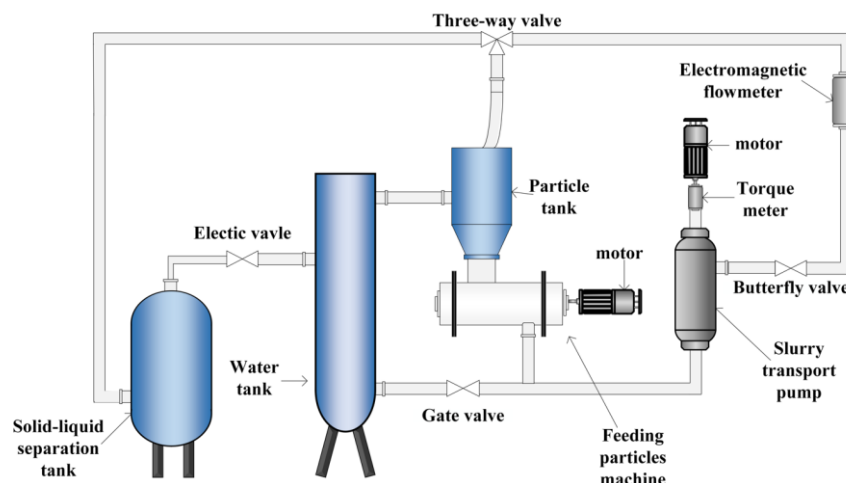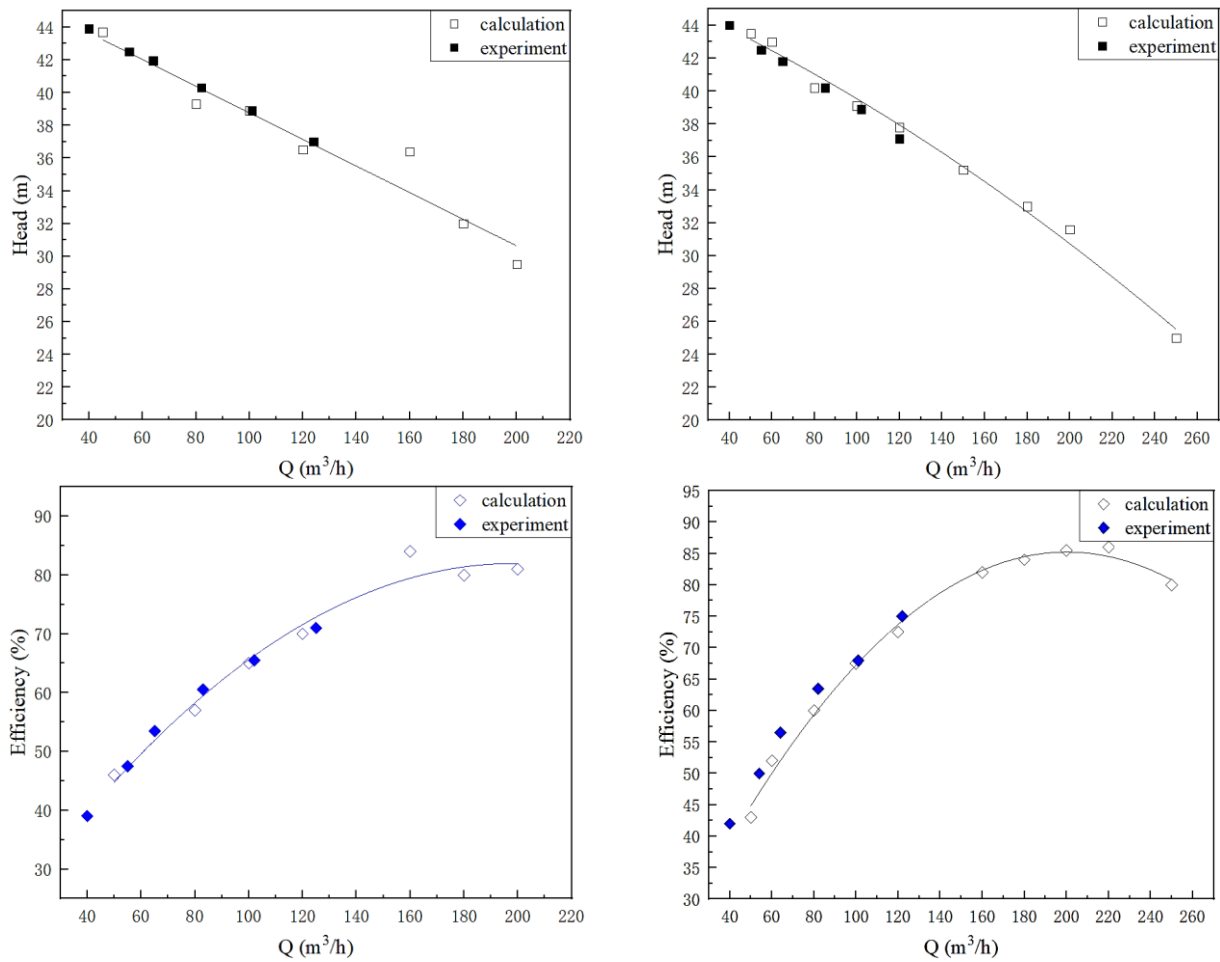**Fig. 10. Experimental measurement system**.

Fig. 11. Schematic diagram of the experimental setup.

(a) Slurry condition   (b) Water condition

Fig. 12. Performance curve of the original transport pump.

Figure 12 presents the experimental and calculated performance curves of the prototype slurry pump under different working conditions. The difference of head and efficiency are 0.51m and 1.98% respectively in the slurry condition; The difference of head and efficiency are 1.72m and 2.50% respectively in water condition. There is little difference between the experimental and simulation values. This proves that the numerical simulation method presented in this article is correct.

3. SIMULATION RESULTS AND DISCUSSION

This section analyzes the particle motion of three different solid–liquid two-phase flow process models. When the transient calculation becomes stable, the calculation data corresponding to the time step of 2.4 s (stable time) was selected for the further study of each model.

3.1 Overall Transportation Performance

In this section, the hydraulic performance of three models with different impeller inlet and outlet area ratios (F2/F1) is compared, as shown in Fig. 13. The ratio of the impeller cross-sectional area (F2/F1) affects the particle-passing capacity. It exerts a negative impact on pump efficiency. When the number increases from 1.57 to 2.51, the pump head space increases in the range of 5–10 m. The efficiency decreases by 5–10% under these conditions.
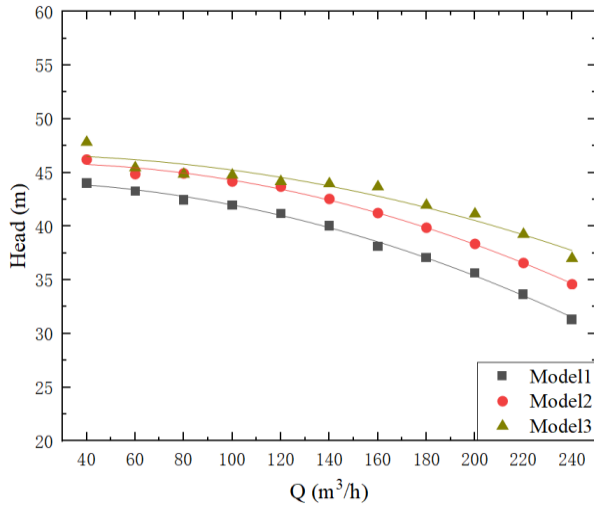
Figure 14 compares the two-level external characteristics of the three models. When the flow rate increases, the difference in efficiency between the two stages first increases and then decreases, and the difference in the efficiency between the two stages reaches a maximum in the range of 5–8% at the actual operating point of 120. The hydraulic loss corresponding to the two stages is compared in Fig. 15. The results show that the total head loss of the two stages decreases with an increase in F2/F1, and this difference decreases as a whole. The head loss difference of model 1 fluctuates, while that for models 2 and 3 remain relatively stable.

3.2 Particle Spatial Distribution

This section presents the influence of different flow areas of the impeller on the movement of internal particles. Agglomeration occurs before the particles enter the impeller, and this can be attributed to low particle velocity, as shown in Fig. 16. When the particles enter the impeller, the speed of the particles increases significantly under the influence of the rotation of the blades. The particles rapidly leave the impeller area, and the maximum speed is attained when they leave the impeller. However, the speed decreases after the particles enter the guide vane, and the particles move smoothly along the suction surface. The particles enter the second-stage impeller at a lower speed in the form of agglomerates. The particle distribution properties in the first and second stages are very similar.

The total number of particles in the original pump reaches a dynamic equilibrium after 0.5s (Fig. 17(a)). The number of particles in the two-stage impeller differs by 2.09%, and the number of particles in the guide vane differs by 1.25% (Fig. 17(b)). Therefore, the particles run smoothly in the pump body without clogging.
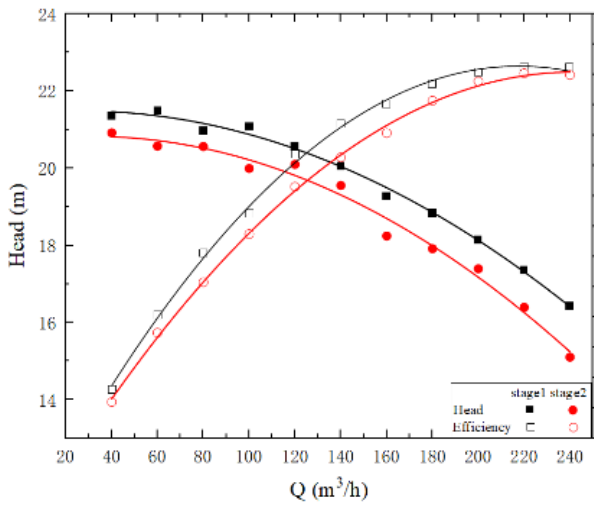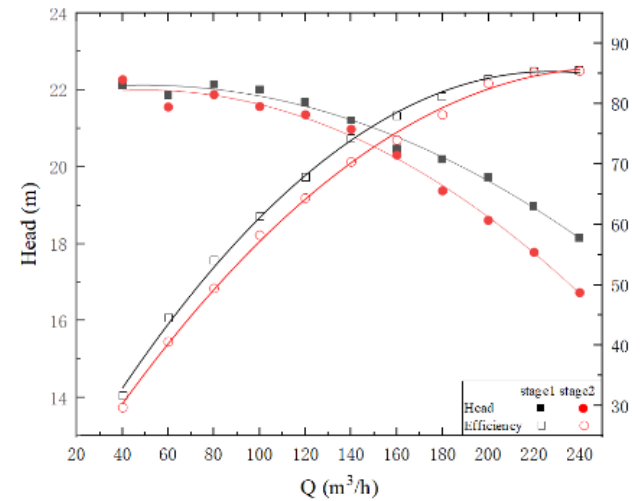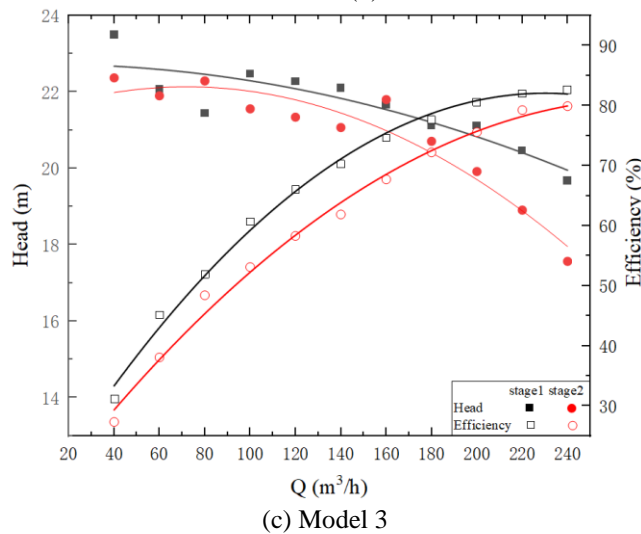

(a) head
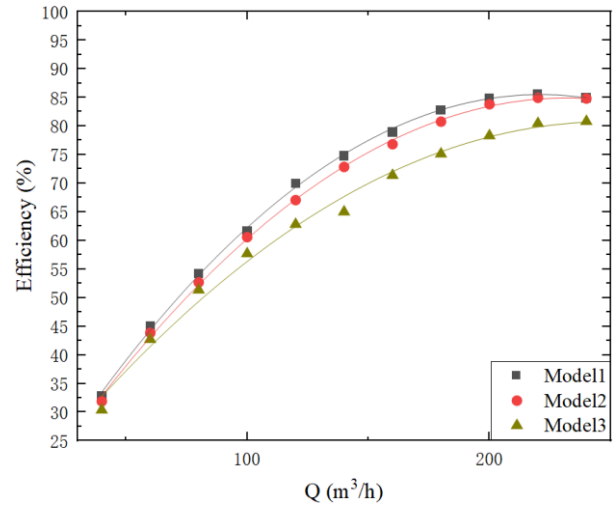
(b) efficiency

Fig. 13. Overall transportation performance.

(a) Model1(original model)

(b) Model 2

(c) Model 3

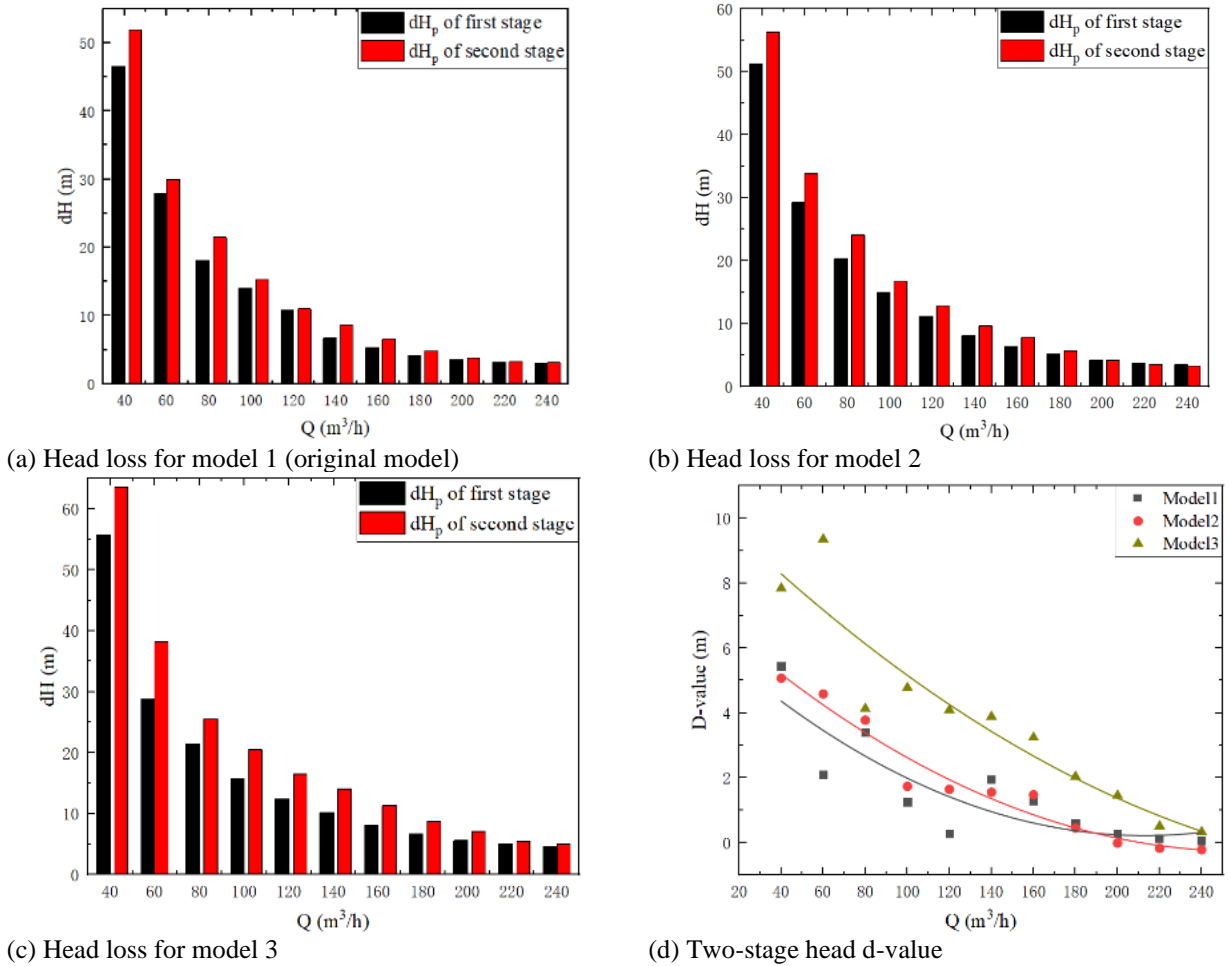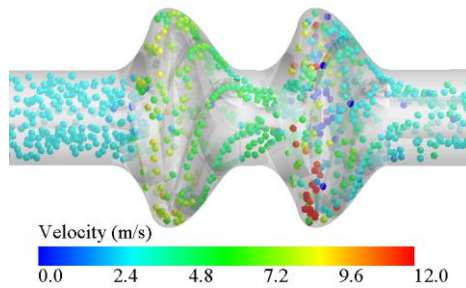**Fig. 14. Comparison of two-level external characteristics.**

(a) Head loss for model 1 (original model)

(b) Head loss for model 2

(c) Head loss for model 3

(d) Two-stage head d-value

Fig. 15. Comparison of two-stage head loss.

Fig. 16. Velocity of particles in the prototype transport pump.

(a) Number of particles in the pump at each time

(b) Proportion of particles in the main components of the pump
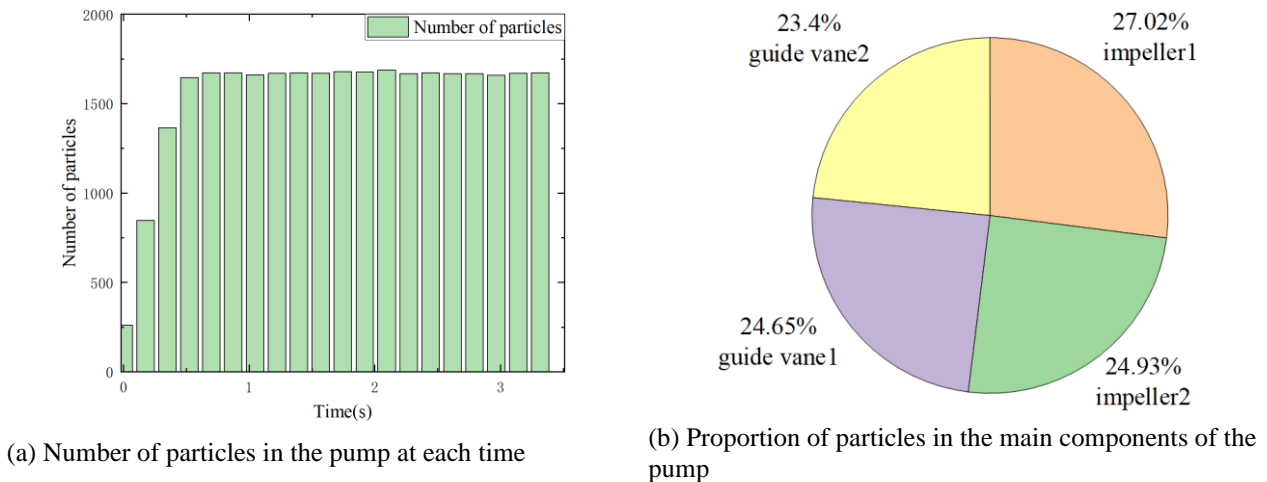
Fig. 17. Quantity distribution of particles in the slurry pump.

(a) Model1(original model)   (b) Model2   (c) Model3
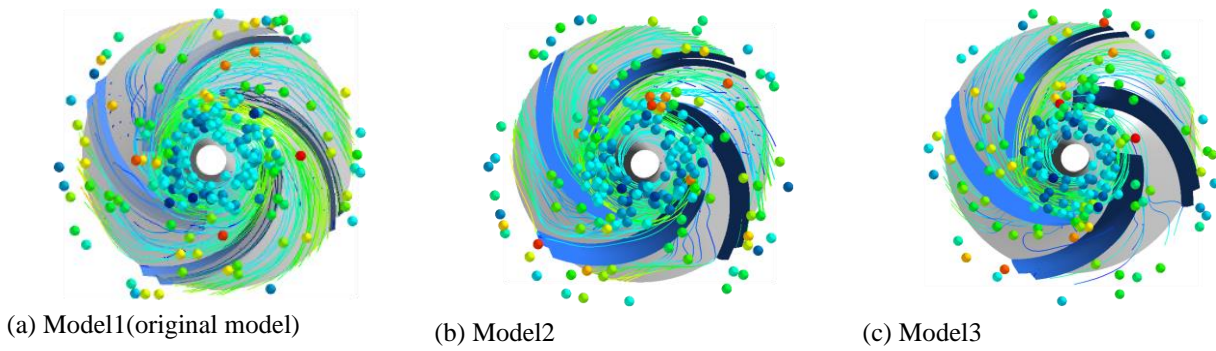
Fig. 18. Particle distribution in the first stage.

(a) Liquid phase velocity of model 1

(b) Particle trajectory for model 1

(c) Liquid phase velocity of model 2

(d) Particle trajectory for model 2   (e) Liquid phase velocity of model 3   (f) Particle trajectory for model 3
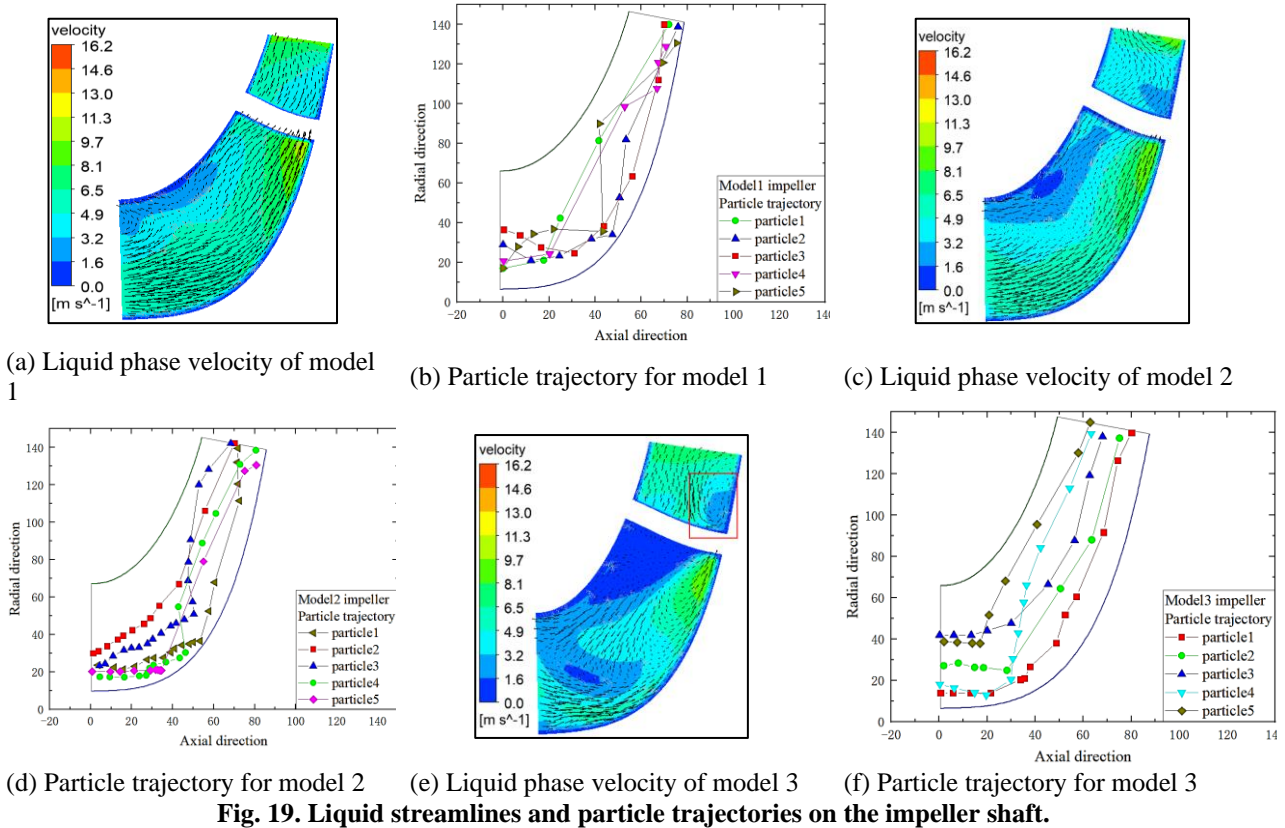
Fig. 19. Liquid streamlines and particle trajectories on the impeller shaft.

Figure 18 presents the velocity and distribution of the particles and the motion direction and trend of the streamlines in the impeller. After the fluid and particles enter the impeller, the direction of fluid flow changes from the vertical (at the input pipe) to the radial. However, the change in direction has little effect on the movement of the particles, and the particles still move along the axial direction. So, the particles form two parts by velocity and degree of aggregation. The particle velocity is low in the area around the central region of the impeller. Hence, the particles crowd and collide with the impeller hub under these conditions. The streamline velocity gradually increases from the central region to the outlet with the rotation of the impeller. This drives particles in the central area outward, and the particles and the water body gradually accelerate and quickly leave the impeller under these conditions. Therefore, the distribution is relatively sparse. However, the particles moving inside the impeller collide with the wall and other particles numerous times, resulting in a large variation in the speed of the particles near the outlet.

As shown in Fig. 19, the change in the flow area of the impeller affects the solid and liquid phases. Five particles were selected from the impellers of three models for trajectory comparison.

It can be seen from Fig. 19(a) that a relatively high-velocity area is found at the hub area and outlet area of the impeller, and the particles move rapidly in this region. For the particles shown in Fig. 19(b), the motion trajectories of the particles interfere with each other and a crowded environment is formed. The particles are close to the inner wall at the outlet. With an increase in F2/F1, the low-velocity area in the middle of the impeller increases significantly as shown in Fig. 19(c) and Fig. 19(e). The backflow phenomenon is observed at the outlet of the impeller under these conditions. Figure 19(e) reveals the formation of a prominent vortex near the red box. Under the influence of the vortex at the outlet, an increase in the extent of dispersion of the particles (Fig. 19(d) and Fig. 19(f)) is observed at the outlet. Figure 19(f) reveals a smooth trajectory that facilitates the movement of the particles.
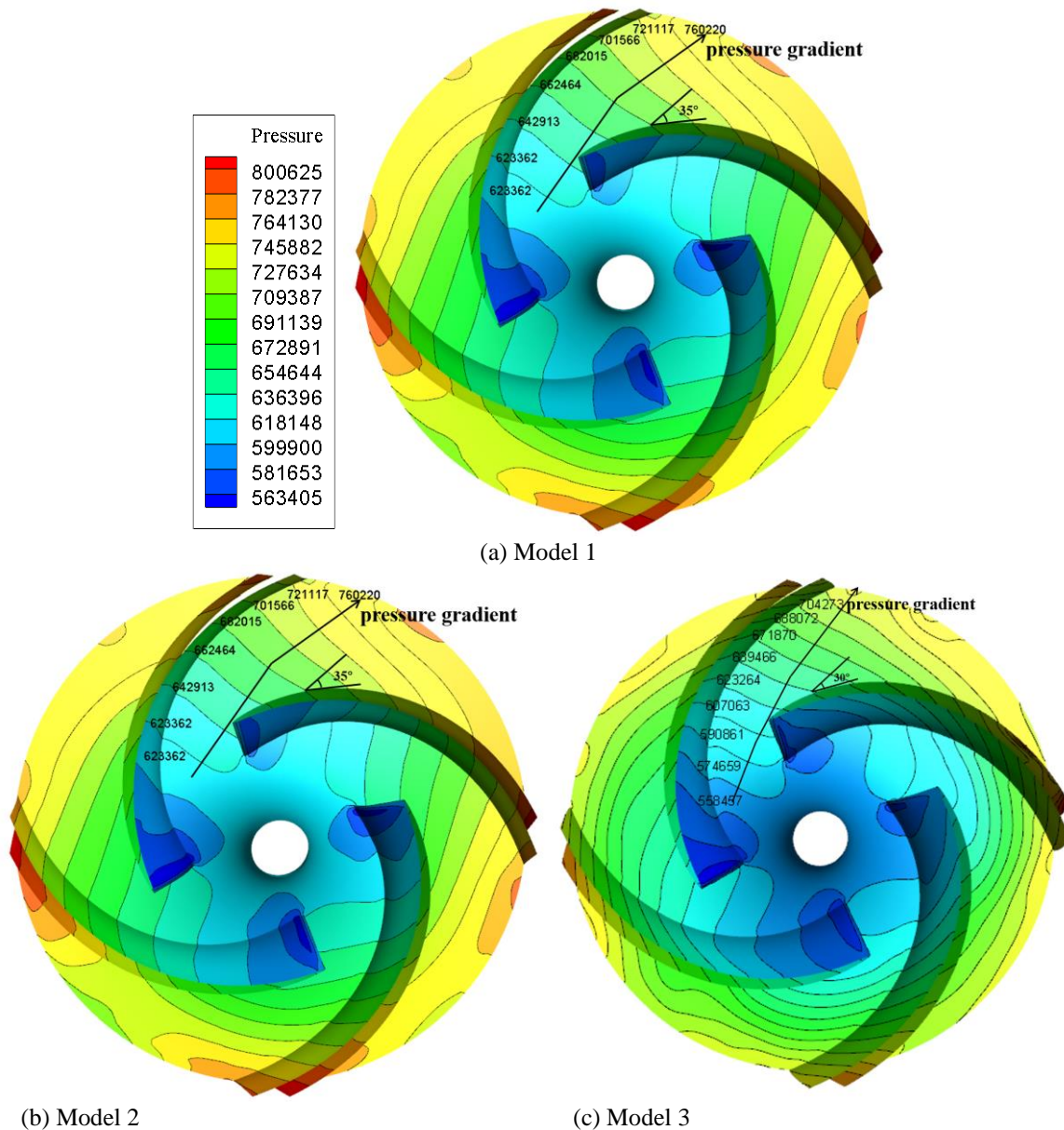
(a) Model 1

(b) Model 2

(c) Model 3

Fig. 20 Pressure distribution inside the impeller.
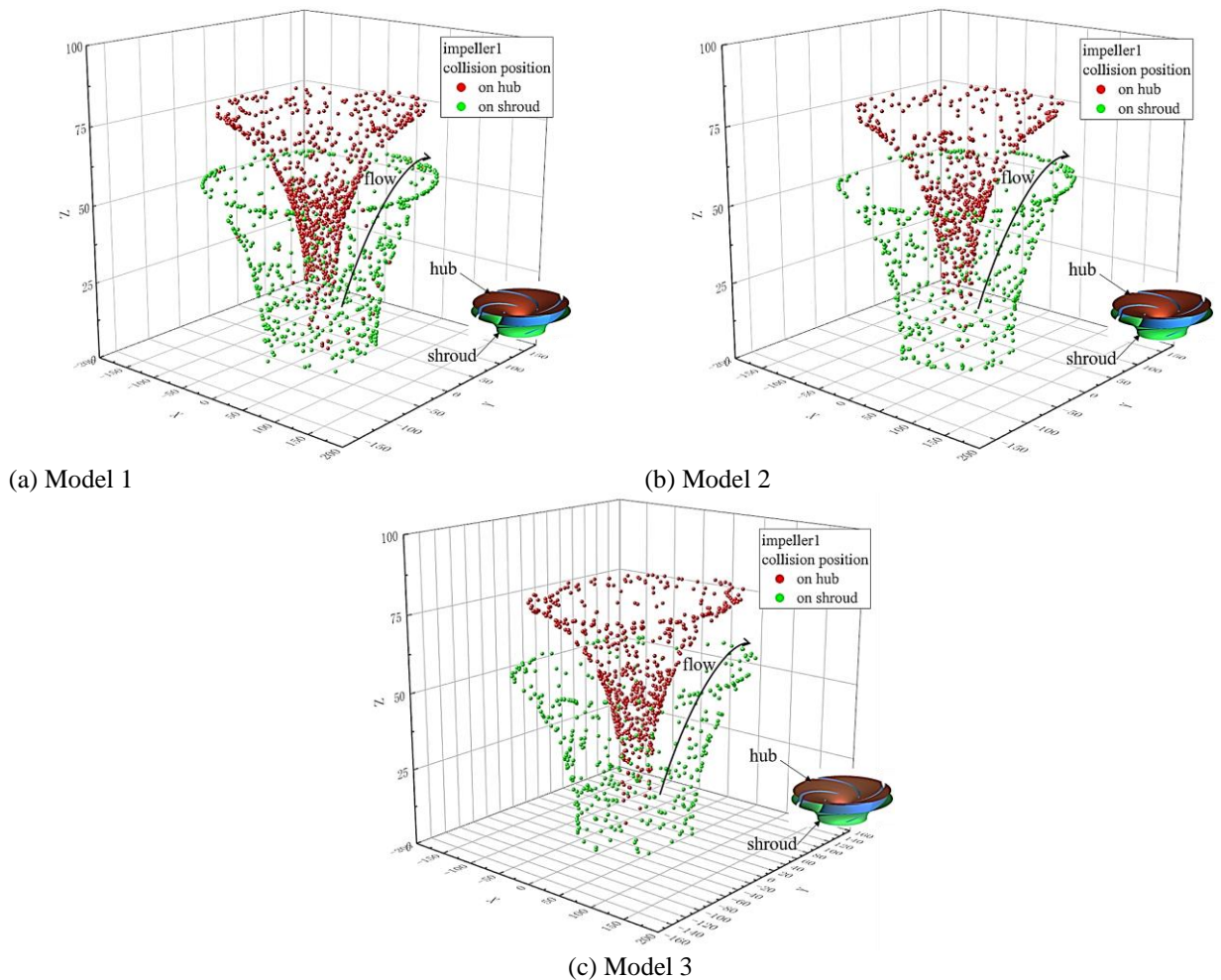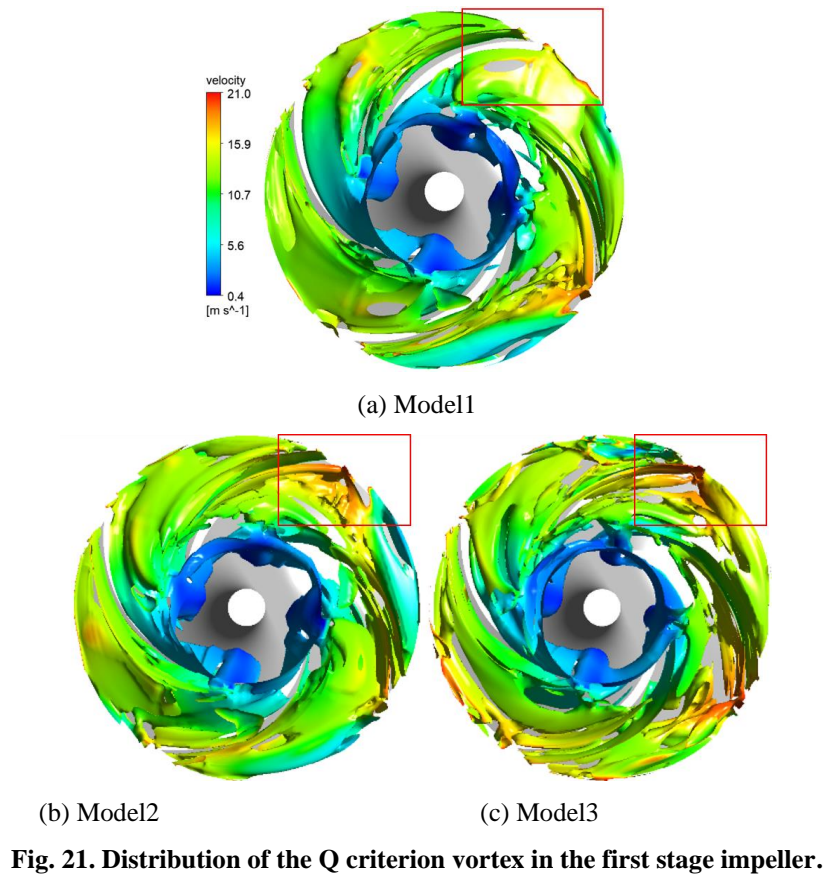
3.3 Flow Field Characteristics

As the impeller rotates, the fluid pressure in the impeller channel increases step by step (Fig. 20). When F2/F1 increased from 1.57 to 2.00, the pressure distribution in the impeller did not change significantly. When the ratio reached 2.51, the overall pressure of the impeller decreased, and the low-pressure area at the inlet became prominent.

The influence of F2/F1 on the pressure and velocity distribution was studied. The vortex structure will be further discussed in the following sections, and the vortex in the flow field will be directly described by the Q criterion (given threshold: Q; Fig. 21). The Q value was set to 0.01, and the vortex intensity coefficient (v value) was used for coloring. The results revealed that the vortex structure and vortex strength changed in the first stage. An increase in the F2/F1 value results in a significant increase in the vortex and size of the red frame area.

3.4 Particle Passing Characteristics

A change in the F2/F1 value results in a change in the collision forms of the particles. The ratio also affects the shroud and the hub in the impeller. Figure 22 presents the collision positions on the shroud (the green dots) and hub (the red dots) of the impeller. Prominent stripes are observed in the particle collision positions in model 1 and model 2 for the impeller shroud structure, and the particle collision positions in model 3 are more random. This can be attributed to an increase in F1/F2, resulting in fewer collisions between the particles and shroud during the acceleration phase. Furthermore, the particles rapidly leave the impeller area under these conditions. As the change in F1/F2 does not change the area of the impeller inlet area, the particle collision positions of the three models are concentrated at the front half of the hub.

Figure 23 presents the proportion of each interval taken by the particles to go through the first-stage impeller. Time is recorded from the instance particles enter the impeller to when the particles leave the impeller.

(a) Model1

(b) Model2

(c) Model3

Fig. 21. Distribution of the Q criterion vortex in the first stage impeller.

(a) Model 1

(b) Model 2

(c) Model 3

Fig. 22. Schematic diagram of the particle-wall collision in the first-stage impeller.
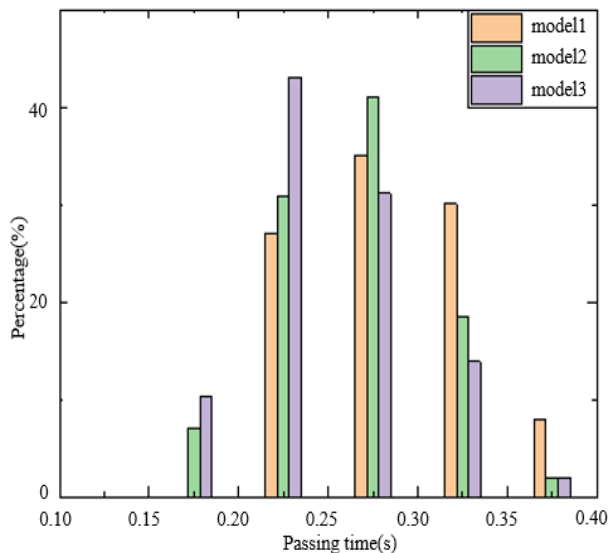
Fig. 23. The proportion of the time period spent by the particles passing through first stage impeller.

The results reveal that the time the particles stay in the impeller changes significantly based on the changes in the F2/F1 values. When F2/F1 increased from 1.57 to 2.00, the proportion of particles with a passing time between 0.2 s and 0.25 s increased from approximately 25 to 43%, while the proportion of the particles with a passing time of more than 3 s decreased gradually.

4. CONCLUSION

This research takes the slurry transport pump and its pumping system as the research object and studies particle motion and the specific correlation between impeller geometry and performance behaviors. The main findings can be summarized as follows:

(1) This paper compares the experimental and simulation results of the external characteristics of the slurry pump. The difference of head and efficiency are 0.51m and 1.98% respectively in the slurry condition; The difference of head and efficiency are 1.72m and 2.50% respectively in water condition, this proves that the experiment is basically consistent with the calculation.

(2) The F2/F1 ratio significantly affects the particle passing capacity but negatively impacts the pump efficiency. When the ratio increases from 1.57 to 2.51, the percentage of particles characterized by the passage interval of 0.2–0.25 s increases from 25 to 43%, while the head space increases in the range of 5–10 m. The efficiency decreases by 5–10% under these conditions. The optimal F2/F1 ratio was in the range of 1.57–2.00, and a satisfying particle passing ability and efficiency can be achieved under these conditions.

(3) Geometric optimizations should consider the contributions from guide vanes and other components, and additional vibration and operational stabilities should also be considered. The hydraulic and structural characteristics of the whole transport system should be comprehensively and quantitatively analyzed in the future to attain a balance between flow efficiency and security.

CONFLICT OF INTEREST STATEMENT

All authors have no conflicts to disclose.

AUTHOR CONTRIBUTIONS:

Zuchao Zhu: Conceptualization, Methodology, Funding acquisition; Yuwei Lv: Writing Original Draft, Visualization, Data Curation; Xianghui Su : Writing Review & Editing, Supervision; J ianyi Z hang Project administration , Resources Runkun Wang: Validation, Investigation; Wenqi Lu: Formal analysis Jiuchun Sun: Data curation

REFERENCES

Abdolahnejad, E., Moghimi, M., & Derakhshan, S. (2021). Experimental and numerical investigation of slip factor reduction in centrifugal slurry pump. *Journal of the Brazilian Society of Mechanical Sciences and Engineering,* 43(4). https://doi.org/10.1007/s40430-021-02831-x

Dong, L., Cheng, T., Ding, S., & Fu, B. (2017). CFD-DEM simulation for distribution and motion feature of crystal particles in centrifugal pump. *International Journal of Fluid Machinery Systems.* 10. https://doi.org/10.5293/IJFMS.2017.10.4.378

Glasby, G. P., Li, J., & Sun, Z. L. (2015). Deep-Sea Nodules and Co-rich Mn Crusts. *Marine Georesources & Geotechnology*, 33(1),72-8. https://doi.org/10.1080/1064119X.2013.784838

Hong, G. J., Zhang, Q. B., & Yu, G. L. (2016). Trajectories of coarse granular sediment particles in a simplified centrifugal dredge pump model. *Advances in Mechanical Engineering,* 8(11). https://doi.org/10.1177/1687814016680143

Kim, Y. I., Kim, S., Yang, H. M., Lee, K. Y., Kim, J. H., & Choi, Y. S. (2019). *Effect of blade thickness on hydraulic performance of a mixed-flow pump impeller.* IOP Conference Series: Earth and Environmental Science, 240(3):032035. https://doi.org/10.1088/1755-1315/240/3/032035

Li, Y. W., Liu, S. J., & Hu, X. Z. (2018). Research on rotating speed's influence on performance of Deep-Sea lifting motor pump based on DEM-CFD. *Marine Georesources & Geotechnology,* 37(8), 979-88.

https://doi.org/10.1080/1064119X.2018.1514550

Li, Y., Liu, S., & Hu, X. (2019). Research on reflux in deep-sea mining pump based on DEM-CFD. *Marine Georesources & Geotechnology,* 38(6), 744-52. https://doi.org/10.1080/1064119X.2019.1632995

Liu, S. J., Yang, H. L., Hu, X. Z., Zhao, H. (2019a, January 12-13). *Influence of the blade angle of guide vane outlet on the performance of lifting electric pump in deep sea mining*. International Conference on Intelligent Transportation, Big Data & Smart City (ICITBS), Changsha, PEOPLES R CHINA2019.

Liu, S. J., Wen, H., Zou, W. S., Hu, X. Z., Dong, Z. (2019b, January 12-13). *Deep-Sea mining pump wear prediction using numerical two-phase flow simulation.* International Conference on Intelligent Transportation, Big Data & Smart City (ICITBS), Changsha, Peoples R China 2019.

Liu, S. J., Li, Y. W., Hu, X. Z., Dai, Y. (2019c, January 12-13). *Prediction of quasi - fluid performance in different volume concentration of deep sea mining*. International Conference on Intelligent Transportation, Big Data & Smart City (ICITBS), Changsha, Peoples R China 2019.

Matlakala, M. E., Kallon, D. V. V., Mogapi, K. E., Mabelane, I. M., Makgopa, D. M. (2019, October 22-25). *Influence of impeller diameter on the performance of centrifugal pumps.* Conference of the South African Advanced Materials Initiative (CoSAAMI), Vanderbijlpark, South Africa 2019.

Sha, Y., & Hou, L. (2012). Effects of blade thickness on performance of axial flow pump and analysis of internal flow field. *Transactions of the Chinese Society of Agricultural Engineering*, 28(18), 75-81.

Sharma, R. (2011). Deep-sea mining: economic, technical, technological, and environmental considerations for sustainable development. *Marine Technology Society Journal,* 45(5), 28-41.

https://doi.org/10.4031/MTSJ.45.5.2

Tang, C., & Kim, Y. J. (2020). CFD-DEM simulation for the distribution and motion feature of solid particles in single-channel pump. *Energies,* 13(19). https://doi.org/10.3390/en13194988

Tao, Y., Yuan, S. Q., Liu, J. R., Zhang, F., & Tao, J. P. (2017). The influence of the blade thickness on the pressure pulsations in a ceramic centrifugal slurry pump with annular volute. *Proceedings of the Institution of Mechanical Engineers Part a-Journal of Power and Energy,* 231(5), 415-31. https://doi.org/10.1177/0957650917708495

Tarodiya, R., & Gandhi, B. K. (2019). Numerical simulation of a centrifugal slurry pump handling solid-liquid mixture: Effect of solids on flow field and performance. *Advanced Powder Technology*, 30(10), 2225-39. https://doi.org/10.1016/j.apt.2019.07.003

Wang, M. H. (2015). *The development of deep seafloor solid mineral resources*. Central South University Press.

Wang, R. K., Zhu, Z. C., Su, X. H., Mianowicz, K., Jia, H., & Wu, K. X. (2022). Slurry pumps in deep-sea mining: A review of numerical and experimental studies. *Ocean Engineering*, 251. https://doi.org/10.1016/j.oceaneng.2022.111150

Wen, H., Liu, S. J., Zou, W. S., Hu, X. Z., Dong, Z. (2019, January 12-13). *Effects of particle diameter on erosion wear characteristic of deep-sea mining pump.* International Conference on Intelligent Transportation, Big Data & Smart City (ICITBS), Changsha, Peoples R China 2019.

Yang, C. X., Dong, F. D., Cheng, X. R. (2013, September 19-22). *Numerical investigation of sediment erosion to the impeller in a double-suction centrifugal pump*. 6th International Conference on Pumps and Fans with Compressors and Wind Turbines (ICPF), Tsinghua Univ, Beijing, Peoples R China 2013.